The Role of the Indonesian Throughflow on ENSO Dynamics in a Coupled Climate Model

A. SANTOSO

Climate Change Research Centre, University of New South Wales, Sydney, New South Wales, Australia

W. CAI

CSIRO Marine and Atmospheric Research, Aspendale, Melbourne, Victoria, Australia

M. H. ENGLAND AND S. J. PHIPPS

Climate Change Research Centre, University of New South Wales, Sydney, New South Wales, Australia

ABSTRACT

The effects of the Indonesian Throughflow (ITF) on ENSO dynamics are studied in a coupled climate model by comparing two simulations, one with an open ITF and the other with a closed ITF. Closing the ITF results in an El Niño–like climate state in the Pacific, which is characterized by weakened trade winds, a flatter equatorial thermocline, and weaker equatorial upwelling. A weakened South Equatorial Current allows the western Pacific warm pool to extend eastward, thereby reducing the zonal temperature gradient along the equator. The interdecadal component of the ENSO-like variability collapses, although the interannual variability is maintained. The core region of the ENSO SST anomalies becomes confined farther east. This results from Bjerknes feedback processes that are shifted eastward. This study conducts an analysis utilizing the Bjerknes coupled stability index as formulated by Jin et al. and finds that the relative importance of the thermocline feedback is enhanced in the closed ITF experiment. This indicates a more prominent ENSO thermocline mode, thus explaining the existence of more prevalent eastward-propagating anomalies. A weaker zonal advective feedback due to the reduced mean zonal temperature gradient contributes to the dominance of the thermocline mode. The strength of the thermocline feedback itself is maintained by enhanced coupling between the zonal wind stress and the east–west thermocline slope. However, an increased thermal damping by air–sea heat flux dominates the overall ENSO feedback process.

1. Introduction

The El Niño–Southern Oscillation (ENSO) is the dominant mode of global climate variability, having a profound worldwide societal impact. Consequently, there have been a vast number of studies investigating the dynamics and predictability of ENSO, yet presenting us still with further challenges and scope for research [see reviews by Neelin et al. (1998), McPhaden et al. (2006), Guilyardi et al. (2009), and Collins et al. (2010)]. Paleoclimate-based studies provide evidence that the strength of ENSO has varied over long time scales and is strongly influenced by the background mean state (e.g., Tudhope et al. 2001; Koutavas et al. 2002; Fedorov et al. 2006). A significant shift to the background climate can be introduced by changes in the mean strength of the Indonesian Throughflow (ITF).

It has been demonstrated using models that the state of the global climate, particularly that of the Indo-Pacific, is dependent to a large extent on the presence of the ITF (e.g., Hirst and Godfrey 1993; Wajsowicz and Schneider 2001; Cane and Molnar 2001; Song et al. 2007; England et al. 2010, manuscript submitted to *J. Climate*). The ITF allows a substantial amount of heat to be transported from the Pacific into the Indian Ocean: on the order of 0.5 PW (Vranes et al. 2002). The ITF annual transport estimates hover around 10 Sverdrups (1 Sv $\equiv 10^6$ m^3 s^{-1}), with substantial seasonal and interannual variations (see Potemra 1999; Gordon 2005; Potemra and Schneider

Corresponding author address: Agus Santoso, Climate Change Research Centre, University of New South Wales, Sydney, NSW 2052, Australia.
E-mail: a.santoso@unsw.edu.au

2007; Wijffels et al. 2008). Furthermore, the ITF is known to vary in phase with ENSO (e.g., Meyers 1996; England and Huang 2005), such that during La Niña (El Niño) years the ITF transport is anomalously high (low). Thus, changes in the configuration of the Indonesian passages, for instance, because of the lower sea level during the Last Glacial Maximum (Voris 2000) or tectonic plate movements (Cane and Molnar 2001), could imply significant climatic changes.

Earlier modeling studies investigated the role of the ITF on the global climate by comparing the mean climate with an open ITF versus that with a closed ITF. The studies using ocean-only models (e.g., Hirst and Godfrey 1993; Lee et al. 2002) and others with coupled models (Schneider 1998; Wajsowicz and Schneider 2001; Song et al. 2007) found, among other things, that blocking the ITF warms the equatorial Pacific. The coupled models, however, exhibit a more prominent El Niño–like warming in the Pacific, compared to the stand-alone ocean models. These SST patterns are a result of positive feedback interactions between the ocean and atmosphere.

ENSO is a coupled air–sea phenomenon involving changes in the trade winds in response to anomalous SST over the equatorial Pacific cold-tongue region and interactions with thermocline depth variations. These interactions constitute a positive feedback as the anomalous winds in effect force anomalous ocean circulation that in turn reinforces the anomalous SST via upwelling—a Bjerknes (BJ) feedback process (Bjerknes 1969). The growth of the anomalous SSTs is limited generally by the damping effect of the air–sea heat fluxes (e.g., Wang and McPhaden 2000). On the other hand, ocean wave dynamics provide the means for a negative feedback mechanism in the termination of ENSO events (e.g., Schopf and Suarez 1988; Battisti and Hirst 1989; Jin 1997). The evolution of warm-water volume above the main thermocline in the equatorial Pacific is an important part of ENSO dynamics. A heat content buildup preconditions El Niño development, followed by a discharge of heat out of the equatorial region as part of the thermocline adjustment process to the anomalous westerlies. This eventually leads to a shallow basinwide thermocline, thus terminating the El Niño event and preconditioning the La Niña phase. This is the essence of the recharge oscillator paradigm for ENSO (Jin 1997) and is confirmed by observations (Meinen and McPhaden 2000). In the context of this study, it is worth noting that Cai et al. (2005) showed that the Indian Ocean takes part in this Pacific recharge and discharge process, which is inhibited in a closed ITF setting. Analysis of the climate response to ITF blocking provides an interesting context for assessing how changes in the Pacific–Indian Ocean gateway influence ENSO dynamics.

Wajsowicz and Schneider (2001) found that blocking the ITF in a coupled model reduces the interannual variability of the equatorial Pacific SST. However, they integrated their coupled model for only 20 yr and thus were not able to resolve a sufficient variety of ENSO events. In contrast, Song et al. (2007) found in a 200-yr integration of a coupled model with a closed ITF configuration that the ENSO exhibits stronger variability in the interannual time band and a shorter period than when the ITF is open. However, they did not proceed to investigate the causes of the altered ENSO characteristics in their model. Such an investigation is the objective of the present study.

In this study, a coupled climate model is implemented to conduct experiments with an open and closed ITF. However, both runs are integrated for longer than 1000 model years to reach a more steady state and to capture a variety of ENSO events. Significant changes to the ENSO characteristics are found in the closed ITF experiment. An explanation of the causes of these changes is provided, particularly, by examining the components that constitute the Bjerknes coupled feedbacks. The rest of the paper is organized as follows. The model and experimental design are described in section 2. An overview of the link between ENSO and ITF transport in the model is also provided in section 2. In section 3, the response of the model to the closure of the ITF is discussed, and the ENSO characteristics are compared between the two experiments. Section 4 is reserved for a further examination of the mechanisms that explain the change in the ENSO dynamics. Finally, a discussion and conclusions are provided in section 5.

2. The climate model

a. Model description and experimental design

This study employs the Commonwealth Scientific and Industrial Research Organisation Mark version 3.0L (CSIRO Mk3L) model, a fully coupled general circulation model (GCM) designed specifically for millennial-scale climate simulations (Phipps 2010). The atmospheric model is a low-resolution version of that used in the Intergovernmental Panel on Climate Change (IPCC)-class CSIRO Mk3 model (Gordon et al. 2002), with zonal and meridional resolutions of 5.6° and 3.2°, respectively, and 18 levels in the vertical. The atmospheric model resolves full annual and diurnal cycles and includes a cumulus convection scheme based on the Met Office scheme (Gregory and Rowntree 1990) coupled to the prognostic cloud scheme of Rotstayn et al. (2000). The sea ice model includes dynamics and thermodynamics as described in O'Farrell (1998). The land surface model is an enhanced

version of the soil–canopy scheme of Kowalczyk et al. (1994) with static vegetation and land surface properties.

The ocean model is a z-coordinate GCM, which is an improved version of that used in the Mk2 model (Hirst et al. 2000) with doubled zonal and meridional resolutions of $2.8°$ and $1.6°$, respectively. There are 21 vertical levels, increasing in thickness with depth. The vertical diffusivity varies as the inverse of the Brunt–Väisälä frequency (Gargett 1984), with a minimum value set at 3×10^{-5} m^2 s^{-1}, except in the top 80 m where this value is increased to 1.5×10^{-4}–2×10^{-3} m^2 s^{-1} to simulate the effects of mixing by surface winds. Convective mixing is parameterized by increasing the diffusivity to 100 m^2 s^{-1} whenever static instability arises. The model implements the scheme of Gent and McWilliams (1990) and Gent et al. (1995) for the transport of tracers by mesoscale eddies. The eddy diffusivity is set to 600 m^2 s^{-1} in the deep ocean but is reduced toward zero in the upper layers as required by continuity. The above diffusivity values are within the range of observed estimates (e.g., Cisewski et al. 2005). The horizontal viscosity varies as the cosine of latitude, with the value at the equator set to 4×10^5 m^2 s^{-1}. The model's coarse resolution requires horizontal viscosity of such order of magnitude to resolve the viscous boundary layer at sidewalls (Bryan et al. 1975). The model parameter values above are chosen to achieve an optimum simulation of the global climate and to minimize numerical noise across model experiments. The coupled model is forced with an atmospheric CO_2 concentration fixed at the preindustrial level of 280 ppm. A flux adjustment that is seasonally varying but fixed from year to year is employed for heat, freshwater, and momentum to ensure a realistic base state and stability of the simulation on millennial time scales.[1]

Two coupled model simulations are carried out: one with an open ITF (ITF$_{open}$) and the other with a closed ITF (ITF$_{clsd}$) wherein a land bridge is imposed across the Indonesian passages. The ITF$_{open}$ is first integrated for 200 yr, at which point the ITF is then blocked (ITF$_{clsd}$). Each of the two experiments is further integrated for 1200 yr. We compare and analyze the last 1000 yr of the ITF$_{open}$ and ITF$_{clsd}$ simulations. As a slight drift is still present, all of the output variables have been detrended prior to conducting further analyses. Note that the flux adjustment is necessarily held constant across

experiments to avoid introducing unphysical effects in the ITF$_{clsd}$ experiments. As discussed in section 5, after examining experiments without any flux adjustment terms, this approach does not influence the overall conclusions of the present study.

The model simulates a reasonably realistic present-day climate. Notable biases, however, exist. The model biases that are related to ENSO are briefly outlined here. The model simulates overly strong trade winds with a double intertropical convergence zone (ITCZ), which are also common biases found in IPCC-class climate models (e.g., Guilyardi et al. 2009). These biases are related to the classical equatorial cold-tongue bias. The model also simulates a diffuse thermocline structure, not surprising given its coarse vertical resolution. The slope of the depth of the 20°C isotherm (D20), however, is comparable to the observed. These biases affect the simulated ENSO variability, as we present in section 3b, with notable differences to the observed. For example, the model ENSO exhibits longer periodicities than the observed 2–7 yr. Furthermore, the core of the ENSO SST variability is concentrated in the Niño-3.4 region (5°N–5°S, 170°–90°W), which is farther west than that seen in observations. However, the model does simulate a good skewness pattern of SST probability distribution, with positive and negative skewness in the eastern and western Pacific, respectively (see Burgers and Stephenson 1999). Observed ENSO variability is seasonally phase locked with highest variability in boreal winter and weakest variability in boreal spring. The model ENSO does exhibit similar seasonal phase locking but with the magnitude of the variability peaking one season too early. Overall the model ENSO variance is weaker than observed, partly because of the stronger than observed seasonal cycle of the tropical Pacific climate and the more diffused thermocline (e.g., Guilyardi 2006).

b. ITF–ENSO connection in ITF$_{open}$

The model simulates an ITF transport of about 21 Sv—larger than the observed upper estimates of $\approx$15 Sv (e.g., Wijffels et al. 2008). This overestimate is largely attributed to the joint effect of baroclinicity and relief (JEBAR). As noted by England et al. (1992), the horizontal streamfunction is exactly determined by three terms: friction terms (wind stress and bottom friction), JEBAR, and nonlinear terms. In non-eddy-resolving models, the nonlinear terms are negligible and bottom frictions are of second order (England et al. 1992). The wind stress component of the ITF transport is known to be well estimated by the island rule of Godfrey (1989), which is close to 12 Sv in ITF$_{open}$. The island rule involves taking a line integral of long-shore wind stress enveloping the west coast of Australia, the southern tip of Tasmania, the west coast

---

[1] The flux adjustment terms are derived as the difference between the monthly heat, freshwater, and momentum fluxes from the atmospheric model and those from the ocean model diagnosed at the end of their spinup phase. There is no restoring toward observations applied during the coupled run. In this sense, the atmosphere and ocean components interact freely within the coupled model.
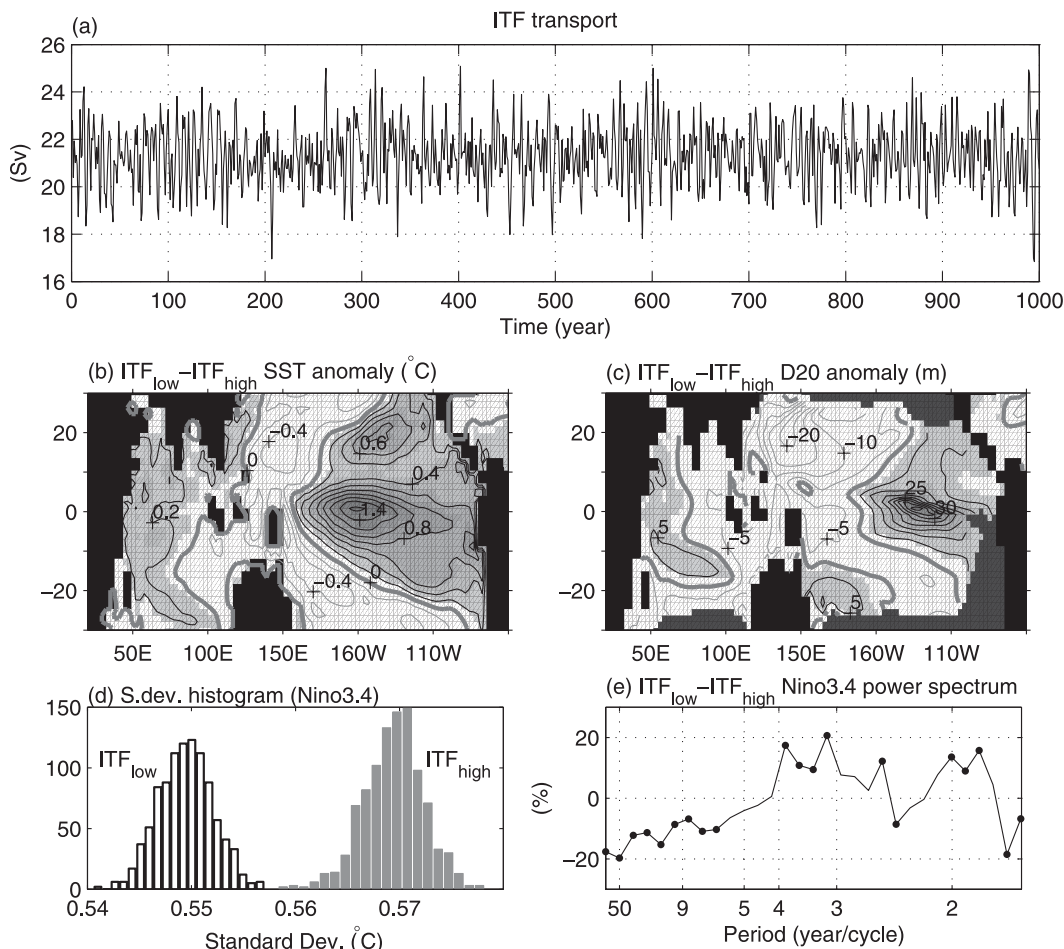
FIG. 1. (a) 1000-yr time series of annual mean ITF transport in the model. Composite differences between years of weak and strong ITF transport on decadal time scales for (b) SST and (c) depth of 20°C isotherm. Positive values in (b) and (c) are contoured in black and shaded in gray, negative values are contoured in gray, and thick gray contours indicate a zero value. (d) A histogram is shown of the bootstrapped mean of Niño-3.4 standard deviation sampled over 50-yr periods during multidecadal epochs of weak (black outlined) and strong (gray) ITF transport. (e) Difference of the sample averaged power spectra between weak and strong ITF transport (in percentage change from strong ITF transport case). Black dots in (e) indicate where the differences are significant over the 95% confidence level by a Student's t test.

of South America, and the northern tip of New Guinea [see Fig. 2 of Godfrey (1996)]. This accounts for the ITF component driven by Sverdrup dynamics, leaving the remaining 9 Sv to be attributable to JEBAR. Differences in ITF sill topography, and the density field on either side of the sill, between the model and observations can contribute to a spurious JEBAR term. The topography differences are symptomatic of coarse-grid models and potentially exacerbate the density differences by forcing the JEBAR term to act across a different density class in the model. Experiments conducted using the ocean model with varying sill depths confirmed that the model's ITF transport is sensitive to the choice of sill depth, a case similar to the model of Hirst and Godfrey (1993), which

is indicative of a JEBAR influence [see also Wajsowicz (1993)]. The model ITF transport nonetheless exhibits year-to-year variability (Fig. 1a) with a standard deviation of 1.3 Sv, consistent with existing observational and modeling studies (e.g., Meyers 1996; England and Huang 2005; Song et al. 2007). Furthermore, the transport variability is significantly correlated to the Niño-3.4 index ($r \approx -0.5$) as observed (e.g., Tillinger and Gordon 2009) with the peak-to-trough ENSO amplitude translating to $\approx$4-Sv ITF range, comparable to the observed 5 Sv estimated by Meyers (1996).

One key component linking ENSO and the ITF transport is the equatorial Pacific zonal winds, which are highly correlated to both the ITF transport ($r \approx 0.7$) and Niño-3.4
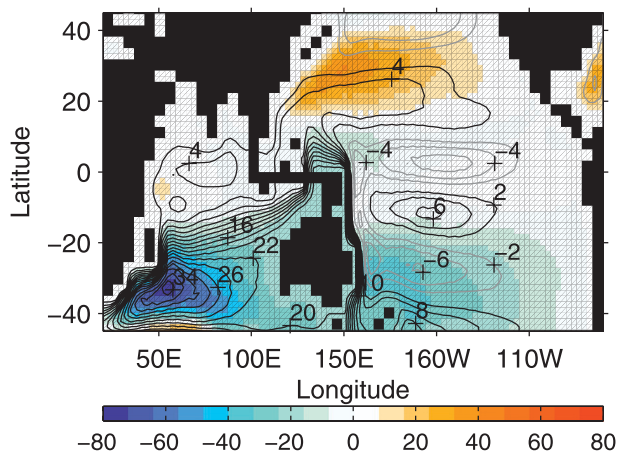
FIG. 2. Difference in horizontal streamfunction between ITF$_{clsd}$ and ITF$_{open}$ experiments shown in contours (contour interval 2 Sv). Black (gray) contours indicate positive (negative) values. The mean ITF$_{open}$ streamfunction is shown in color contrasts.

($r \approx -0.8$) in the model [using basinwide-averaged zonal wind stress (τ^x)]. These correlations are strongest over interannual-to-decadal time scales. As a result, composites depicting El Niño conditions emerge during epochs of weak ITF transport and trade winds, with warm SST and a flatter equatorial thermocline in the Pacific (Figs. 1b,c). These relationships are also found in nature, and their properties appear to evolve against the backdrop of multidecadal trends (McPhaden and Zhang 2002; Wainwright et al. 2008; Feng et al. 2010). In the model, the ENSO amplitude tends to be weaker and of higher frequency during the multidecadal epochs of weak trade winds and ITF transport (Figs. 1d,e).

The analyses described above provide evidence that the ITF and ENSO are closely linked in the model, a feature that is particularly relevant for the purpose of this present study. As we will see below, closing the ITF introduces a significant alteration to climate, impacting on ENSO characteristics in a fundamental way.

3. Response to ITF blocking

a. Mean climate

Blocking the ITF immediately alters the large-scale ocean circulation as shown in Fig. 2, which presents the difference in the depth-integrated circulation fields between ITF$_{clsd}$ and ITF$_{open}$. The cyclonic streamfunction anomaly enveloping the eastern coast of Australia and the southwestern Indian Ocean depicts a shutting down of the ITF transport, a stronger East Australian Current, and a weakened Agulhas Current. These changes have been reported in previous studies using both ocean-only

and coupled models. However, the multigyre response in the Pacific appears to be a feature of a coupled feedback response associated with wind stress changes [see also Wajsowicz and Schneider (2001)].

The changes in wind stress and sea level pressure (SLP) over the tropical Pacific Ocean are presented in Figs. 3a,b. Westerly wind anomalies develop along the equator east of the date line, in response to the high and low pressure anomalies set up in the west and east, respectively. This surface pressure response stems from changes in SST (Fig. 3c), with warming in the eastern Pacific and cooling in the west (as also found by Wajsowicz and Schneider 2001; Song et al. 2007). The SST anomalies are in turn linked to a deepened thermocline in the east and a raised thermocline in the west (Fig. 3d), implying a flatter thermocline slope along the equator, consistent with the weakened trade winds. The equatorial warming and cooling signals become more pronounced when considering temperature averaged over the entire upper 300 m (Fig. 3e). This is because the temperature changes are related to changes in the thermocline depth where vertical temperature gradients are large. The net air–sea heat flux field shows an opposite sign to that of SST (Fig. 3f), thus acting in response to the SST rather than driving the SST anomalies. These results are qualitatively consistent with previous studies using coupled GCMs (Wajsowicz and Schneider 2001; Song et al. 2007), however, with a modestly stronger response.

Figure 4a presents the mean vertical velocity at 50 m in ITF$_{open}$ exhibiting equatorial upwelling in the Pacific. The differences in the vertical velocity and surface currents between ITF$_{clsd}$ and ITF$_{open}$ are shown in Fig. 4b. Consistent with the weakened trade winds, the equatorial upwelling in the central Pacific is reduced. The westward South Equatorial Current is also weakened as marked by the eastward current anomalies. This allows the western Pacific warm pool to intrude eastward, on average, thus weakening the zonal temperature gradients. The westerly wind anomalies also act to weaken the surface ocean meridional divergence. By geostrophy, the flattening of the equatorial thermocline weakens the meridional convergence below the Ekman layer (not shown). Overall, there is a weak anomalous discharge of the equatorial thermocline, with the warm-water volume in ITF$_{clsd}$ about 8% smaller than that in ITF$_{open}$.[2] This volume change is substantial, considering the changes involved in the ENSO recharge–discharge in ITF$_{open}$ are on the order of 3% from the climatological mean.

---

[2] The warm-water volume is calculated by integrating the depth of the 20°C isotherm over the Pacific basin between 5°S and 5°N [see also Meinen and McPhaden (2000)].
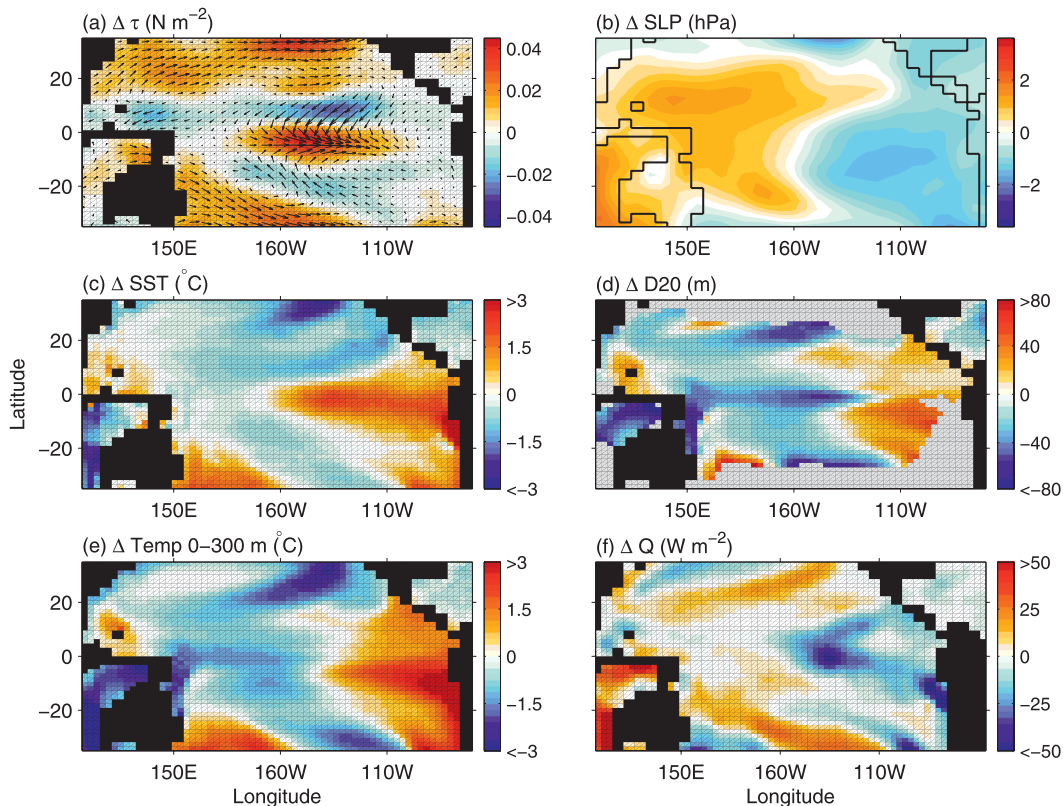
FIG. 3. Annual mean difference in ocean and atmospheric fields between ITF$_{clsd}$ and ITF$_{open}$ showing the following: (a) surface wind stress τ shown in vectors and the zonal component in color; (b) SLP; (c) sea surface temperature; (d) D20; (e) temperature averaged over the top 300 m; and (f) net air–sea heat flux Q. The sign convention for air–sea heat fluxes is positive for downward and negative for upward.

It is apparent that the response to ITF closure involves a coupling between the ocean and atmosphere. The weakened trade winds are linked to the eastern Pacific warming accompanied by a flatter thermocline—a scenario depicting a weakened Walker circulation. In addition, the ITCZ shifts southward as inferred from Fig. 5, which shows the latitudinal profiles of the zonally averaged wind stress in ITF$_{open}$ and ITF$_{clsd}$ averaged over the Pacific Ocean. The changes described above depict a shift toward a more El Niño–like climate state.

b. ENSO characteristics

Closing the ITF results in dramatic changes to the spatial and temporal characteristics of ENSO in the model. The temporal and spatial characteristics of ENSO in ITF$_{open}$ and ITF$_{clsd}$ are extracted by applying a standard empirical orthogonal function (EOF) analysis to the Pacific Ocean SST between 30°S and 30°N. The spatial patterns for the first EOF are shown in Fig. 6, depicting a "classical" ENSO SST in ITF$_{open}$. EOF2 in both ITF$_{open}$ and ITF$_{clsd}$ (not shown) resembles what is commonly termed "ENSO Modoki" (e.g., Ashok et al. 2007; Taschetto and England 2009; Cai and Cowan 2009). In

this study, the focus is on the classical ENSO as represented by EOF1.

As shown in Figs. 6a,b, closing the ITF results in the core of the ENSO SST anomaly becoming confined to the Niño-3 region (5°N–5°S, 150°–90°W). The corresponding principal component (PC) time series (Figs. 6c,d) describing the temporal evolution of the EOF1 pattern is highly correlated ($r > 0.95$) with SST variability at the centers of action: Niño-3.4 for ITF$_{open}$ and Niño-3 for ITF$_{clsd}$. Thus, the SST time series at these regions can be taken as an alternative to represent the leading mode of ENSO variability. The term "ENSO SST" is hereafter used to refer to the SST over these corresponding core regions in ITF$_{open}$ and ITF$_{clsd}$. The power spectra of the principal component time series are shown in Figs. 6e,f. While the ITF$_{clsd}$ ENSO overall exhibits weaker variance than in ITF$_{open}$, closing the ITF alters the ENSO periodicity dramatically (Fig. 6f). The interdecadal variability collapses, but the higher-frequency components of the interannual variability are retained. Note that there are no significant shifts to the seasonal phase locking of ENSO variability in ITF$_{clsd}$ compared to ITF$_{open}$.

FIG. 5. Latitudinal profile of zonally averaged annual mean zonal wind stress over the Pacific basin in ITF$_{clsd}$ (solid line) and ITF$_{open}$ (dashed line).
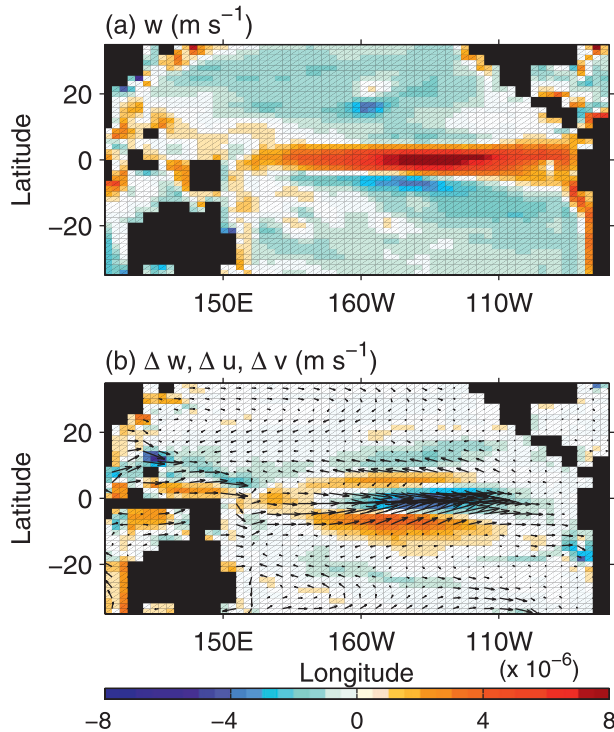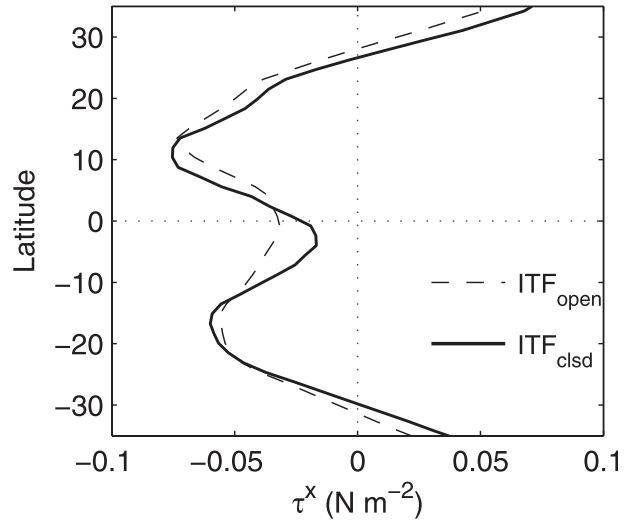

FIG. 4. (a) Annual mean of ocean vertical velocities at 50-m depth in ITF$_{open}$. (b) Annual mean difference in vertical (color map) and horizontal (vectors) velocities between ITF$_{clsd}$ and ITF$_{open}$.

The ENSO in ITF$_{clsd}$ features more prominent eastward-propagating SST anomalies compared to ITF$_{open}$. This is apparent in Figs. 7a,b showing Hovmöller diagrams of SST anomalies along the equator in ITF$_{open}$ and ITF$_{clsd}$ over a selected 50-yr period. The direction of the anomaly propagation can also be diagnosed by applying a lag-correlation analysis between an ENSO SST index and a basinwide zonal SST difference along the equator. As in Trenberth and Stepaniak (2001), the Niño-3 index is taken for the former, and the Trans Niño index (TNI) is adopted for the latter [see also Guilyardi (2006) for a similar analysis]. The TNI is formed by subtracting the Niño-4 (5°N–5°S, 160°E–150°W) index from Niño-1.2 (0°–10°S, 90°–80°W). Thus, a lag-correlation analysis showing Niño-3 leading TNI indicates the existence of eastward-propagating SST anomalies. The opposite holds for westward-propagating anomalies. As upwelling off South America (over the Niño-1.2 region) is simulated in the model (see Fig. 4a), so the use of the TNI in the analysis is appropriate. The lag correlations for the whole 1000-yr model time series are presented in Fig. 7c indicating eastward propagation in both ITF$_{open}$ and ITF$_{clsd}$. However, the much higher correlation coefficients for ITF$_{clsd}$ suggest higher incidences of eastward-propagating anomalies than

in ITF$_{open}$ throughout the 1000-yr simulation. Adopting Niño-3.4 instead of Niño-3 or replacing the TNI with other equatorial basinwide zonal SST differences in the analysis above does not alter this conclusion.

Changes in the direction of propagating anomalies carry dynamical significance (e.g., Fedorov and Philander 2001). Eastward-propagating anomalies have been shown to characterize strong El Niño events such as those observed in 1982/83 and 1997/98 and are generated remotely involving off-equatorial Rossby waves in the discharge and recharge of the equatorial thermocline. Since 1980, in association with a tendency for stronger El Niño events, the off-equatorial Rossby waves are involved in the ENSO discharge and recharge process, a process absent in the pre-1980 period (Shi et al. 2007). On the other hand, westward-propagating ENSO SST anomalies are generated locally via zonal advection and Ekman pumping forced by anomalous winds. The ENSO remote mode (also often referred to as the thermocline mode) tends to be stronger and of longer period than the local mode.

However, the ENSO variability in ITF$_{clsd}$ is found to be generally more rapid and weaker than that in ITF$_{open}$. Guilyardi (2006) found a negative correlation between ENSO amplitude and the strength of the equatorial Pacific seasonal cycle in the IPCC Fourth Assessment Report (AR4) models. However, we find no notable change in the strength of the seasonal cycle when the ITF is closed. As shown in the next section, the change in ENSO characteristics is related to changes in the underlying air–sea coupling, which are in turn linked to changes in the background mean climate.
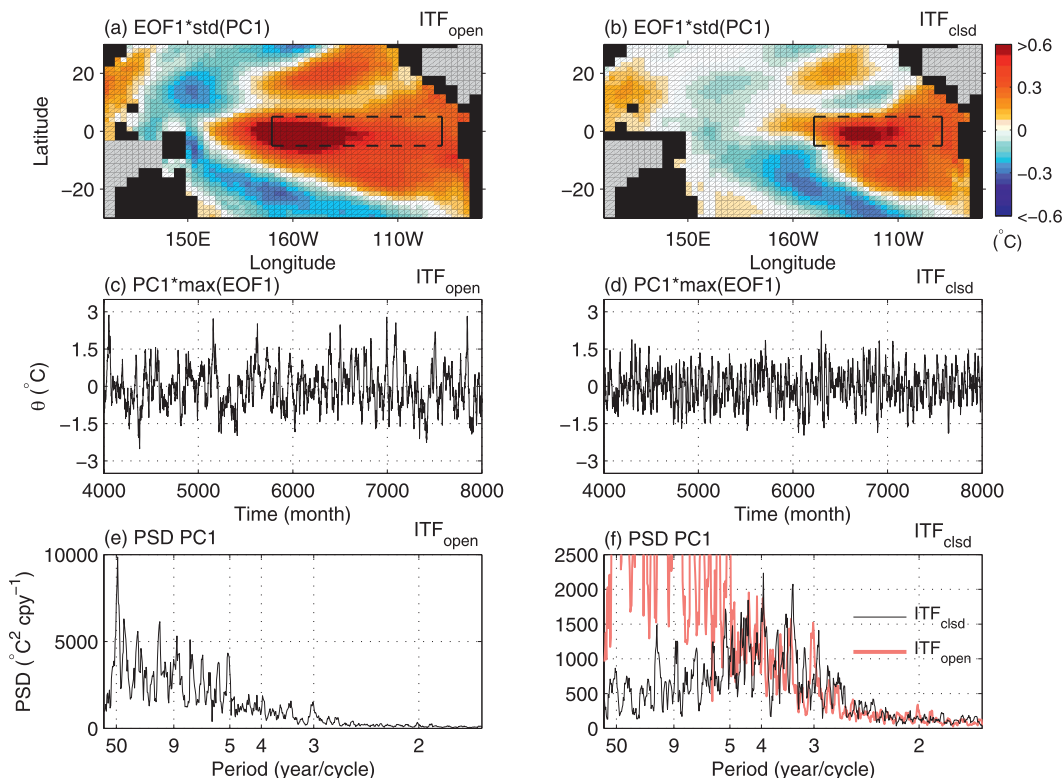
FIG. 6. EOF analysis of SST showing the most dominant mode, which represents 32% and 18% of the total data variance for (left) ITF$_{open}$ and (right) ITF$_{clsd}$, respectively. The whole 1000 yr of monthly data with the seasonal mean removed have been used for the analysis. (a),(b) SST anomalies represented by the first mode that are obtained by multiplying the EOF with the standard deviation of the PC. (c),(d) 330-yr portion of SST anomaly time series at the highest EOF1 loading (i.e., within Niño-3.4 in ITF$_{open}$ and Niño-3 in ITF$_{clsd}$). (e),(f) Power spectral density (PSD) of the principal component time series. In (f), the PSD for ITF$_{open}$ (light red) is overlaid onto that of the ITF$_{clsd}$ (black). Note the smaller y-axis range in (f) to enhance the visibility of the ITF$_{clsd}$ PSD. The dashed boxes in (a) and (b) indicate the regions used for the stability analysis in section 4.

4. Changes to the ENSO dynamics

To understand how the ENSO characteristics become altered, we first inspect the surface heat budget components that correspond to the zonal advective, Ekman pumping, and thermocline feedbacks driving the growth of ENSO SST anomalies. These are, respectively, the zonal advection of mean temperature by anomalous current ($u'\overline{\theta}_x$), vertical advection of the mean temperature by anomalous upwelling ($w'\overline{\theta}_z$), and vertical advection of temperature anomalies by the mean upwelling ($\overline{w}\theta'_z$). The regression coefficients of the advection terms against the ENSO SST anomalies in ITF$_{open}$ and ITF$_{clsd}$ are shown in Fig. 8. A positive (negative) regression coefficient can be interpreted as a contribution of the corresponding advection term to the SST anomaly growth (decay) rate [see Santoso et al. (2010) for a discussion on this particular form of a heat budget analysis]. In ITF$_{open}$, the zonal advection ($u'\overline{\theta}_x$) and anomalous upwelling ($w'\overline{\theta}_z$) terms contribute to the growth of SST anomalies in the Niño-3.4

region where the SST variability is largest (see section 3b). The vertical advection term ($\overline{w}\theta'_z$) is associated with the growth of SST anomalies farther east, and it contributes to the phase transition in the west. In ITF$_{clsd}$, all of the advection terms become more localized farther east within the Niño-3 region, contributing to the anomaly growth there.

The eastward shift in the advection terms manifests from changes in variability of the zonal currents, upwelling, and stratification. This is demonstrated in Figs. 9a–c, which present the difference in the standard deviation of ocean surface zonal velocity u, vertical velocity w, and vertical temperature gradient θ_z at the surface in ITF$_{clsd}$ and ITF$_{open}$. A zonal dipole pattern is seen in all of the standard deviation difference fields, exhibiting enhanced variability in the Niño-3 region and weakened variability westward. A similar dipole pattern is found in the difference of the standard deviation of the zonal wind stress (Fig. 9d), indicating a coupling between the ocean and atmosphere. The dipole pattern found in the various fields

(a) ITF$_{open}$

(b) ITF$_{clsd}$

(c) TNI vs Nino3
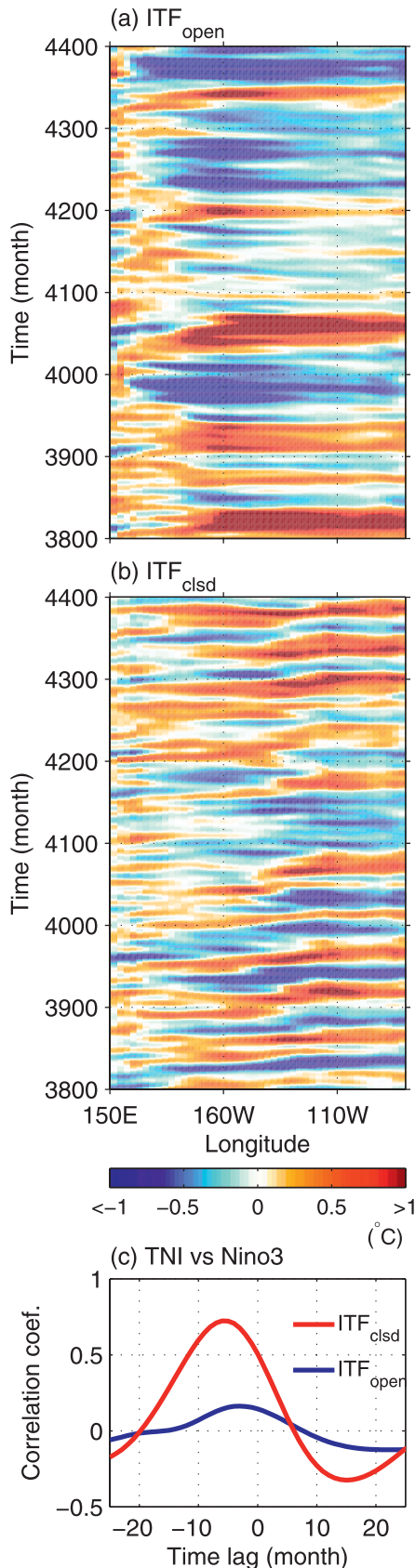
depicts an eastward shift in climate variability as part of an integrated response to the changes in the background climate (section 3a). Figure 10 presents a lag-correlation analysis between the ENSO SST time series (see section 3b), the zonal wind stress, and the thermocline depth in both ITF$_{open}$ and ITF$_{clsd}$. The analysis illustrates a Bjerknes feedback relationship that is displaced eastward in ITF$_{clsd}$. The more rapid variability with a higher ENSO frequency in ITF$_{clsd}$ is apparent in the shorter-correlation time lags. A further analysis is required to understand the characteristics of the ENSO dynamics because the mechanisms for ENSO phase change and damping may be convolved in the advection terms for ENSO SST shown in Fig. 8 (Kang et al. 2001). Below, we implement an analysis that isolates the components of the advection terms that are dynamically linked to ENSO growth.

Jin et al. (2006) formulated a BJ coupled stability index for the thermodynamic equation of ENSO SST in which dynamical relationships based on the recharge–oscillator paradigm are incorporated. The BJ index provides a measure of linear stability for ENSO SST evolution, indicating a growth rate if positive and a decay rate if negative [see Eq. (9) in Jin et al. (2006)]. Negative contributions to the BJ index come from the collective effect of the mean advection and upwelling (denoted hereafter as BJ$_1$) and thermal damping by net air–sea heat flux (BJ$_2$). Positive contributions come from the zonal advection (BJ$_3$), Ekman pumping (BJ$_4$), and thermocline feedbacks (BJ$_5$). Each of the advection feedback terms is a function of the coupling strength between the oceanic variables (i.e., surface currents and thermocline depth) and the zonal wind stress (τ^x), which is in turn coupled to the ENSO SST anomalies. As shown by Jin et al. (2006), this forms the basis of the following formulation:

1) the zonal advection feedback term is a product of the sensitivity of the local τ^x response to the ENSO SST anomalies (denoted by μ_a), the sensitivity of the zonal ocean current velocity response to local τ^x (β_u), and the climatological zonal temperature gradient ($\bar{\theta}_x$);

←

FIG. 7. Hovmöller plots of monthly equatorial SST anomalies in (a) ITF$_{open}$ and (b) ITF$_{clsd}$ over a selected 50-yr period. High-frequency variability shorter than 1 yr has been filtered out. (c) Lag correlation between the TNI and the Niño-3 in ITF$_{clsd}$ (red) and ITF$_{open}$ (blue) for the 1000-yr data. Negative (positive) time lags indicate Niño-3 leading (lagging) TNI. The TNI is constructed as Niño-1.2 (0°–10°S, 90°–80°W) minus Niño-4 (5°N–5°S, 160°E–150°W). Thus, positive (negative) correlations at negative (positive) time lags indicate an eastward propagation of SST anomalies.
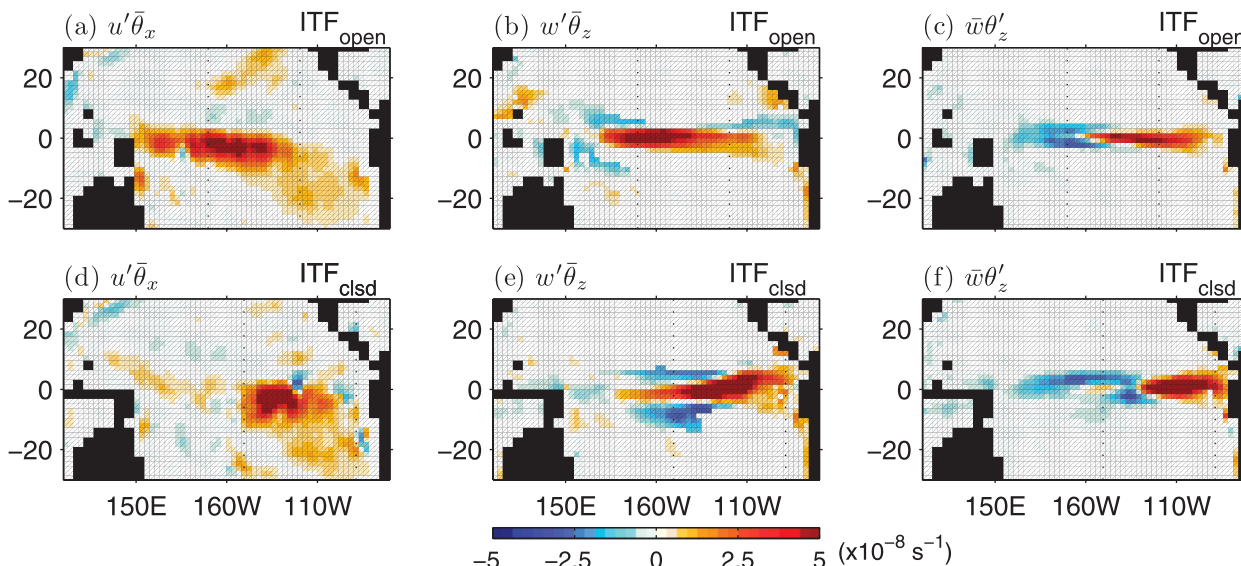
FIG. 8. Advection terms regressed onto the ENSO SST anomalies in (a)–(c) ITF$_{open}$ and (d)–(f) ITF$_{clsd}$. See text for definition of terms.

2) the Ekman-pumping feedback term is a product of μ_a, the sensitivity of local upwelling response to local τ^x (β_w), and the climatological vertical temperature gradient ($\bar{\theta}_z$); and

3) the thermocline feedback term is a product of the sensitivity of the response of the zonally averaged τ^x to the ENSO SST anomalies (μ_a^*), sensitivity of the east–west thermocline slope response to the zonally integrated τ^x (β_h), and the local mean upwelling velocity ($\bar{w}$).

Following Jin et al. (2006), we calculate the above parameters in both ITF$_{open}$ and ITF$_{clsd}$ using the SST equation averaged over the area where most of the ENSO variability resides. Thus, we consider the warm anomaly over the equatorial region (5°S–5°N) spanning 170°–89°W for ITF$_{open}$ and a smaller region eastward, 150°–89°W, for ITF$_{clsd}$ (see Figs. 6a,b). We consider the upper 50 m of the ocean for the calculations, and we estimate the sensitivity parameters via linear regression using the 1000-yr annually averaged model data. The results are presented in Tables 1–3, suggesting a damped system in both ITF$_{open}$ and ITF$_{clsd}$ as indicated by a negative BJ index. However, the ITF$_{clsd}$ ENSO is more strongly damped given the more negative BJ index. This is consistent with the higher frequency and weaker ENSO in ITF$_{clsd}$ compared to ITF$_{open}$ (see section 3b). The main contributor to the increased damping in both experiments is the air–sea heat flux (BJ$_2$). A secondary contribution comes from the weaker positive feedback terms (BJ$_3$, BJ$_4$, and BJ$_5$). The reduction in the other damping term (BJ$_1$), as associated with the anomalous El Niño–like climatological currents in ITF$_{clsd}$ (Fig. 4b), moderates the overall increased damping rate.

As shown in Fig. 7 (section 3b), eastward-propagating SST anomalies become more prominent in ITF$_{clsd}$. This suggests an increased prominence of the thermocline mode. Table 2 compares the ratio of BJ$_5$ to [BJ$_3$ + BJ$_4$] in ITF$_{clsd}$ and ITF$_{open}$. This comparison detects the change in the strength of the thermocline feedback relative to the zonal advective and Ekman-pumping feedbacks. Indeed, there is about a 20% increase in the relative importance of the thermocline feedback, indicating an increase in the prominence of the thermocline mode in ITF$_{clsd}$. When we conduct the stability analysis as described above but now with a bandpass filter applied to separate interannual and interdecadal variability, the increase in the relative strength of the thermocline mode is found to be more dramatic (66%) on the interannual time scales over which most of the ITF$_{clsd}$ ENSO variability resides (Table 2). On interdecadal time scales, the relative importance of the thermocline mode is reduced (Table 2). This is because the thermocline mode is more dominant on the interdecadal time scales in ITF$_{open}$. It is further noted that the increased prominence of the thermocline feedback in ITF$_{clsd}$ is mostly due to the weakened zonal advective feedback on interannual time scales, and to a lesser extent, the Ekman-pumping feedback (Tables 1 and 2). Nonetheless, these dynamical changes are not as pronounced as the damping by the net air–sea heat flux that occurs over interannual-to-interdecadal time scales.

Further inspection of the BJ index component parameters (Table 3) reveals that the strength of the thermocline feedback in ITF$_{clsd}$ is maintained by an increased coupling (β_h) between the zonal thermocline tilt and the zonally averaged zonal wind stress. This occurs
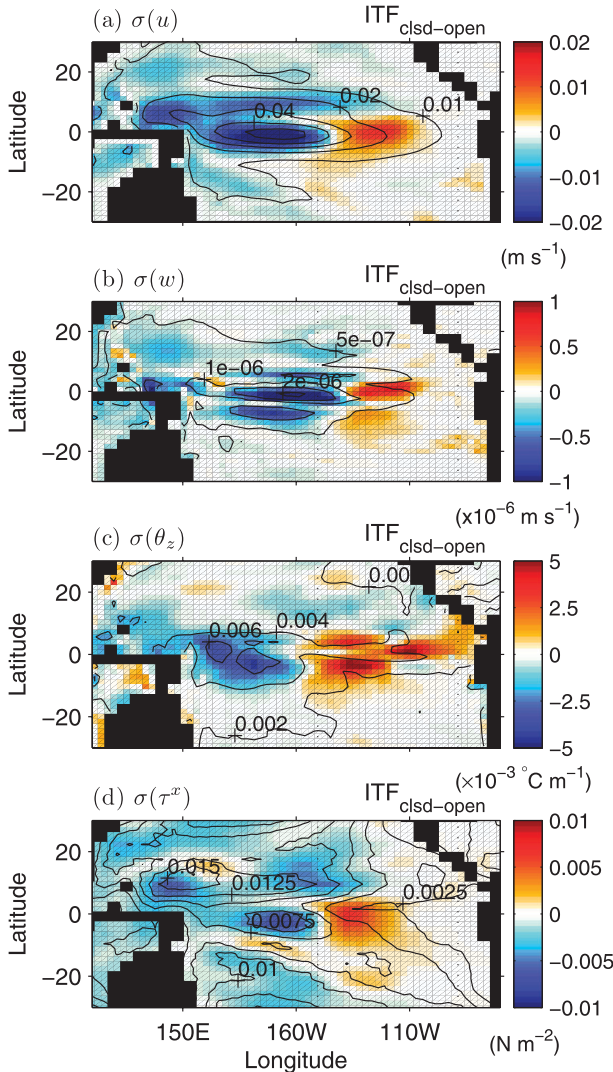
FIG. 9. The difference in the standard deviation between ITF$_{clsd}$ and ITF$_{open}$ (color) for (a) u, (b) w, (c) θ_z, and (d) τ^x. The standard deviations of the ITF$_{open}$ variables are contoured. The dotted lines mark the Niño-3 longitudes. The zonal velocity is the average for the top 50 m, w is at 25-m depth, and θ_z is calculated using the difference between the temperature average of the top 50 m and the next model level at 65-m depth.

amidst the reduction in the mean upwelling ($\overline{w}$) and the sensitivity in the response of the zonally averaged τ^x to the ENSO SST (μ_a^*). On the other hand, the weakened zonal advection feedback is due to a reduced coupling (β_u) between the zonal currents and the local τ^x, as well as the weaker zonal temperature gradient ($\overline{\theta}_x$). The slightly weakened Ekman-pumping feedback is due to a reduced coupling (β_w) between the upwelling and the local τ^x, amidst an increase in surface stratification ($\overline{\theta}_z$). The reduction in these local feedback processes is, however, offset by an enhanced sensitivity of the local τ^x

to the ENSO SST (μ_a), which may be expected given the warmer average SST in ITF$_{clsd}$ (section 3a). Warmer SSTs provide more moisture for latent heating than colder SSTs owing to the nonlinear relation between SST and the saturation mixing ratio via the Clausius–Clapeyron relation, thus providing the condition for stronger air–sea coupling (see, e.g., Neelin and Held 1987; Knutson and Manabe 1995). This also explains why the air–sea heat flux damping is stronger in ITF$_{clsd}$.

The ENSO internal wave dynamics are known to be linked to the spatial structure of the τ^x anomalies (e.g., Kirtman 1997; Capotondi et al. 2006). The sensitivities of the τ^x anomalies to the ENSO SST in ITF$_{open}$ and ITF$_{clsd}$ are shown in Fig. 11. The τ^x anomalies in ITF$_{clsd}$ exhibit broader meridional structure and a center of mass that is shifted eastward. These τ^x anomaly patterns project onto the thermocline depth anomalies. Figure 12 presents the spatial patterns of the two most dominant EOF modes of the D20 variability. In both ITF$_{open}$ and ITF$_{clsd}$, EOF1 captures the equatorial discharge/recharge action, with its PC time series being highly correlated to the warm-water volume along the equator ($r \approx 0.8$ in both ITF$_{open}$ and ITF$_{clsd}$). The ITF$_{clsd}$ EOF1 exhibits broader meridional extent but with limited longitudinal extent to the east of the date line (Figs. 12a,c). EOF2, on the other hand, depicts the zonal tilt variations, with an apparent eastward shift in ITF$_{clsd}$ compared to ITF$_{open}$ (Figs. 12b,d). These patterns are consistent with the change in the atmospheric circulation described above.

The relationships between the D20 modes and ENSO SST are shown in Figs. 12e,f via a lag-correlation analysis. The shorter lead–lag-correlation period for EOF1 in ITF$_{clsd}$ (Fig. 12e) implies that the recharge and discharge process is more rapid in ITF$_{clsd}$ compared to ITF$_{open}$ (see also Figs. 10b,d for the time lags of highest correlations between the warm-water volume and ENSO SST). Similarly, the second mode in ITF$_{clsd}$ also exhibits a shorter lead–lag correlation period (Fig. 12f). These results are consistent with the shorter time that would be required to discharge and recharge the smaller volume of warm water in ITF$_{clsd}$ (see section 3a). This is consistent with the shift in the relative importance of the thermocline feedback, from interdecadal-to-interannual time scales.

As the speed of Rossby waves decreases poleward, it is generally expected that broader meridional extent of τ^x would generate slower off-equatorial Rossby waves, thus resulting in a longer ENSO period (e.g., Kirtman 1997). Furthermore, An and Wang (2000) demonstrated that an eastward shift in the τ^x anomalies can enhance ENSO variability and prolong its period, via an enhanced zonal advective feedback. The zonal advective feedback is actually weakened in the ITF$_{clsd}$ experiment because of a reduced zonal temperature gradient. Neither of these
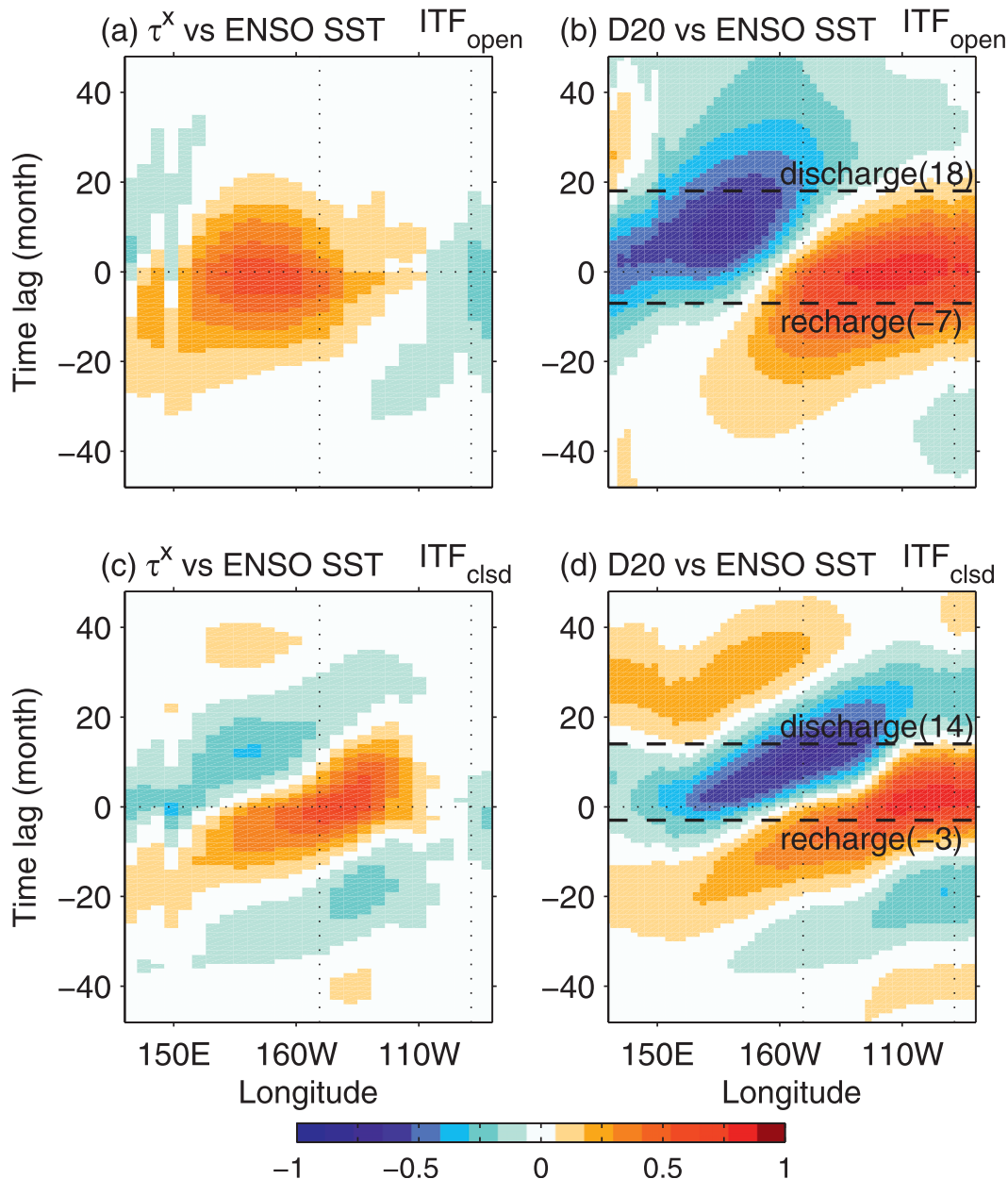
FIG. 10. Lag-correlation analysis between ENSO SST (see Fig. 6) and the (left) zonal wind stress and (right) D20 along the equator for (top) ITF$_{open}$ and (bottom) ITF$_{clsd}$. Positive (negative) time lag indicates ENSO SST leading (lagging) the other variables. The time lags at the highest correlations ($|r| > 0.4$) between ENSO SST and the warmwater volume (volume of water above D20 across the equatorial Pacific; see section 3a) are indicated by dashed horizontal lines in (b) and (d), corresponding to phases of discharge and recharge of the equatorial Pacific thermocline. The Niño-3 longitudes are indicated by the dotted vertical lines.

explanations can account for the generally weaker and more rapid ENSO variability seen in the ITF$_{clsd}$ experiment, even though a more prominent thermocline mode is found in ITF$_{clsd}$. This is because the air–sea heat flux becomes a stronger damping agent, as revealed by our analysis, which is associated with the surface warming response in the east.

5. Discussion and conclusions

This study implements a fully coupled climate model to examine the changes in ENSO characteristics due to a climate shift that results from a blocked ITF. In its unperturbed control state, the model exhibits substantial ITF transport variability that is dynamically linked to

TABLE 1. Contributions to the BJ coupled stability index (Jin et al. 2006) computed from the 1000-yr annual mean variables in ITF$_{open}$ and ITF$_{clsd}$. See text (section 4) and Jin et al. (2006) for the calculation of the parameters. The differences between ITF$_{clsd}$ and ITF$_{open}$ are presented in terms of the percentage change from the ITF$_{open}$ values. The BJ stability indices (BJ$_{total}$) are shown in the far-right column. The largest contribution for each experiment and the corresponding difference are shown in bold.

	BJ$_1$	BJ$_2$	BJ$_3$	BJ$_4$	BJ$_5$	BJ$_{total}$
ITF$_{open}$ ($\times 10^{-7}$ s^{-1})	−0.40	**−0.44**	0.16	0.13	0.16	−0.37
ITF$_{clsd}$ ($\times 10^{-7}$ s^{-1})	−0.31	**−0.76**	0.10	0.12	0.14	−0.70
ITF$_{clsd}$ − ITF$_{open}$ (%)	22	**−73**	−39	−9	−11	−88

TABLE 2. Percentage change in the importance of ENSO thermocline mode relative to the local mode from ITF$_{open}$ toward ITF$_{clsd}$. We define the relative importance as the ratio of the thermocline feedback term to the zonal advective and Ekman-pumping feedback terms: BJ$_5$/(BJ$_3$ + BJ$_4$). The calculations are also shown for an analysis using high-pass-filtered data for interannual variability (<10-yr periodicities) and low-pass-filtered data for decadal time scales and beyond. The largest percentage change is shown in bold.

	Raw	<10 yr	>10 yr
ITF$_{clsd}$ − ITF$_{open}$ (%)	20	**66**	−47

ENSO SSTs and the Pacific trade winds on interannual-to-decadal time scales, as seen in the real system (e.g., Feng et al. 2010). The overall model response to a blocked ITF is qualitatively consistent with previous studies (e.g., Wajsowicz and Schneider 2001; Song et al. 2007). The ITF$_{clsd}$ simulation exhibits an El Niño–like climate state change with warming and cooling in the eastern and western Pacific, respectively. This is accompanied by weakened trade winds, a flatter and shallower equatorial thermocline, and weaker equatorial upwelling. The South Equatorial Current is also weakened, allowing the western warm pool to intrude eastward, thus weakening the zonal temperature gradient along the equator.

The ENSO in the ITF$_{open}$ simulation exhibits prominent interdecadal variability and a core SST situated in the Niño-3.4 region. Upon closure of the ITF, the overall ENSO interdecadal variability collapses, but the higher-frequency interannual variability (<5 yr) is maintained. The core of the ENSO SST anomalies becomes confined to the east within the Niño-3 region. Furthermore, eastward-propagating SST anomalies along the equator become a more prominent feature in the ITF$_{clsd}$ simulation. Examination of the ocean advection terms that are important for ENSO reveals an eastward shift in these thermal components, thus explaining the shift in the ENSO SST pattern. An eastward shift also occurs in the variability of the zonal currents, upwelling, and stratification. A similar pattern is also found in the zonal wind stress variability. This suggests an integrated response to a Bjerknes feedback process that is displaced eastward.

To further explain the dynamics that take place in ITF$_{clsd}$, we computed the BJ coupled stability index as formulated by Jin et al. (2006) and analyzed its components. The Jin et al. (2006) formulation allows for an examination of the ENSO growth rate in terms of air–sea coupling and the background climate, within the framework of the recharge–oscillator paradigm. We found that the importance of the thermocline feedback relative to the zonal advective and Ekman-pumping feedbacks is enhanced in ITF$_{clsd}$. This occurs more strongly on the

interannual time scales over which most of the ITF$_{clsd}$ ENSO variability resides. This is accompanied by a reduction in this relative importance on interdecadal time scales over which the thermocline feedback is more prominent in ITF$_{open}$. The shift in time scale is supported by the fact that a shorter time is required to discharge and recharge a smaller volume of warm water in ITF$_{clsd}$. This would also be facilitated by an increased inflow of the Mindanao Current feeding the equatorial Pacific thermocline, as previously suggested by Song et al. (2007). Weaker local feedback processes, particularly the zonal advective feedback, contribute to the enhanced importance of the thermocline feedback in ITF$_{clsd}$. This is due to the weaker mean zonal temperature gradient and to the reduced momentum coupling in ITF$_{clsd}$, which may be expected given the weaker trade winds and ocean current strength in that experiment. The strength of the thermocline feedback itself is maintained by enhanced coupling between the zonally integrated zonal wind stress and the east–west thermocline tilt. This occurs despite the reduced mean upwelling in ITF$_{clsd}$. It is not clear, however, what causes this increased coupling. Further experiments are required to address this issue. Nonetheless, the increased importance of the thermocline feedback in ITF$_{clsd}$ suggests a more prominent thermocline mode underlying the ENSO dynamics in that run. This is consistent with the existence of more prevalent eastward-propagating SST anomalies in ITF$_{clsd}$. An increased damping by air–sea heat fluxes, however, dominates the ENSO SST response to ITF closure, thus favoring the higher-frequency ENSO variability in ITF$_{clsd}$. This increased damping is expected

TABLE 3. Sensitivity parameters and climatological fields averaged over the ENSO SST regions shown in terms of a percentage change in ITF$_{clsd}$ from ITF$_{open}$. See text (section 4) for details. Note that all of the original values are positive, so positive (negative) change indicates stronger (weaker) values in ITF$_{clsd}$.

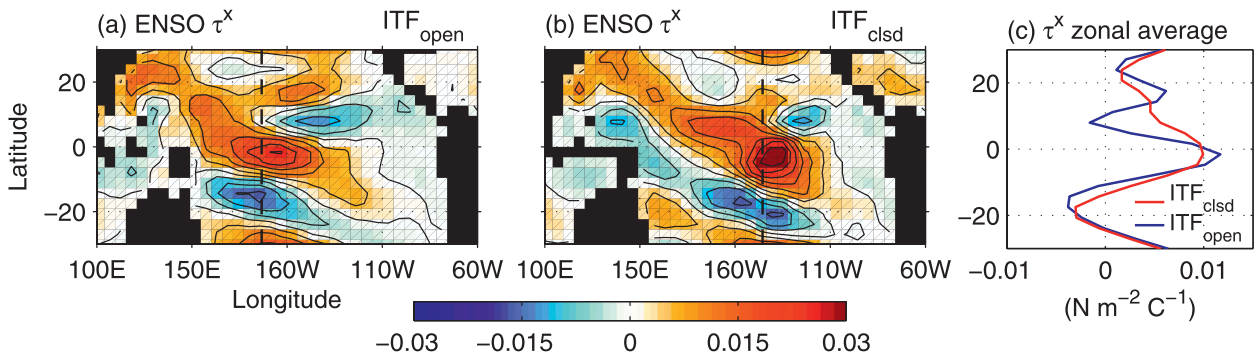|	μ_a	β_u	$\overline{\theta}_x$	β_w	$\overline{\theta}_z$	μ_a^*	β_h	$\overline{w}$
ITF$_{clsd}$ − ITF$_{open}$ (%)	120	−58	−33	−68	31	−12	36	−26

FIG. 11. Surface zonal wind stress regressed onto the ENSO SST anomalies in (a) ITF$_{open}$ and (b) ITF$_{clsd}$. The corresponding center of mass in the regression coefficients along the equator is indicated by the dashed vertical line in (a) and (b). (c) The zonally averaged regression coefficients in (a) and (b) are shown in red for ITF$_{clsd}$ and blue for ITF$_{open}$.

given the warmer average SST in the eastern Pacific in the ITF$_{clsd}$ experiment.

The model employs flux adjustment terms to simulate a realistic control-state climate. While flux adjustment has been suggested to partially suppress climate variability in models (e.g., Pierce et al. 1995), Duffy et al. (2000) used an analysis of 17 climate simulations with and without

flux adjustments to suggest there is no evidence of an impact on temperature variability. To assess whether our results are dependent on flux adjustments, we carried out ITF$_{open}$ and ITF$_{clsd}$ runs without the flux adjustment terms. The nonflux-adjusted ITF$_{open}$ simulates an ENSO-like variability, although weaker and with the core of ENSO SST located farther west over the Niño-4
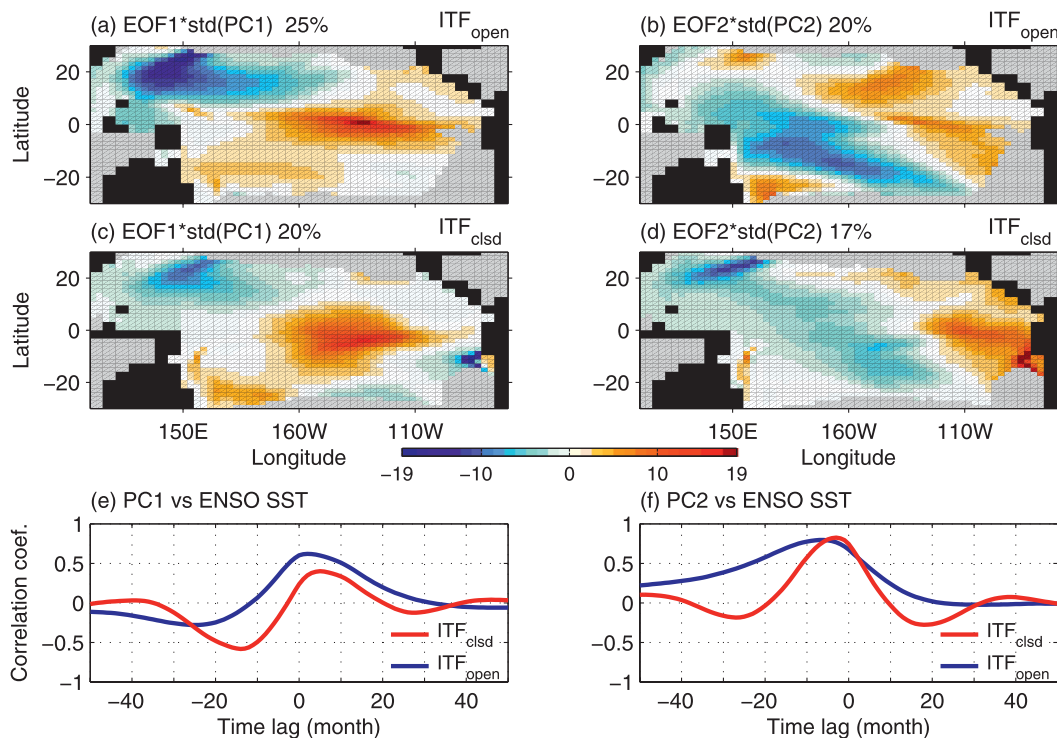

FIG. 12. The first two most dominant EOF modes of D20 in (top) ITF$_{open}$ and (middle) ITF$_{clsd}$. The values are shown with the actual physical unit (meters). This is done by multiplying the EOFs with the standard deviation of the principal components, each appropriately scaled such that the magnitude of the spatial patterns is equivalent to the standard deviation of the D20 anomalies as reconstructed from the corresponding EOF modes. The percentage of total variance explained by each EOF is shown in each panel. (bottom) Lag correlation between (e) the first and (f) the second principal component of D20 and the ENSO SST (principal component of EOF1 for SST; see Fig. 6) for ITF$_{clsd}$ (red) and ITF$_{open}$ (blue). Positive (negative) time lag indicates PC1 leading (lagging) ENSO SST.
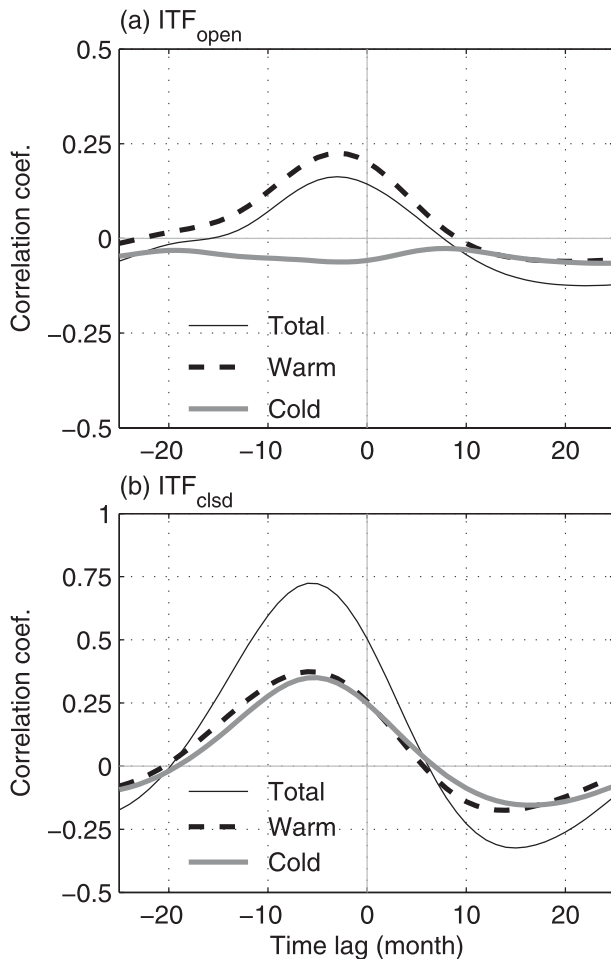
FIG. 13. Decomposition of the total lag correlations between the TNI and Niño-3 in (a) ITF$_{open}$ and (b) ITF$_{clsd}$ (solid black curve; as presented in Fig. 7c) into warm (black dashed) and cold (solid gray) contributions. The warm and cold contributions are separated by computing the respective covariance according to positive and negative Niño-3 anomalies.

region (not shown). This is not surprising given that the nonflux-adjusted climate drifts away from observations. However, closing the ITF in this case still yields many of the key features documented above—namely, a shift toward a more El Niño–like mean climate, an eastward shift of the ENSO patterns, a stronger air–sea damping, weaker ENSO interdecadal variability, an enhanced thermocline feedback process, and more prominent eastward-propagating SST anomalies. This suggests that our results are not significantly influenced by the fixed flux adjustment terms employed. This is likely because the model's atmosphere and ocean components still freely interact even in the presence of flux adjustments, and so physical factors rather than the flux adjustments are more important in setting the model's ENSO response to ITF closure.

It is worth noting that multidecadal epochs of weak ITF transport in ITF$_{open}$ also tend to exhibit a more El Niño–like climate and weaker interdecadal ENSO variability than that seen during epochs of strong ITF transport (see section 2b). However, these tendencies are weaker than those seen in the difference between ITF$_{clsd}$ and ITF$_{open}$ owing to the much greater recirculation and stronger air–sea feedback in ITF$_{clsd}$. In some sense, the ITF$_{clsd}$ case can be seen as an extreme scenario of conditions in ITF$_{open}$ when the ITF transport is weak. However, this should be viewed with caution—for instance, the baroclinic effects of the ITF are naturally absent in ITF$_{clsd}$, whereas they can be substantial in ITF$_{open}$, even when the barotropic transport tends toward zero (Song et al. 2007). The effects of ITF baroclinicity on ENSO are not presently well understood. Nevertheless, the similar tendencies suggest that the ITF$_{clsd}$ experiment may depict some of the underlying mechanisms linking ENSO dynamics to periods of weak ITF transport. These mechanisms should be examined further, particularly across a suite of climate models and parameters to assess the extent to which they are model dependent.

The ITF gateway has evidently been altered in the past. For instance, the low sea level during glacial times could have resulted in a reduced ITF transport (e.g., Kuhnt et al. 2004). However, the Pacific climate was also colder during these periods, so that ENSO behavior would likely contrast that described here (e.g., Lea et al. 2000; Tudhope et al. 2001; Koutavas et al. 2002), making it difficult to draw direct comparisons with our simulations. On the other hand, sometime around the Pliocene period, tectonic changes displaced the northern tip of New Guinea northward, thus narrowing the ITF to the present-day configuration (Cane and Molnar 2001). Interestingly, modeling studies show that the meridionally wider ITF configuration likely yielded slightly weaker ITF transport (Rodgers et al. 2000; Jochum et al. 2009). In this Pliocene setting, these studies found a larger inflow of cold North Pacific thermocline water into the western Pacific, flattening the equatorial Pacific thermocline. In addition, Jochum et al. (2009) found an SST warming in the central Pacific and a weaker ENSO in their Pliocene experiment. These conditions are somewhat analogous to those seen in our study, and so it would be intriguing to conduct a dynamical analysis in the Pliocene setting to examine the extent to which the ENSO feedback processes described here could have also taken place during that epoch.

The direction of ENSO SST zonal propagation can be useful for detecting the underlying dominant feedback processes regulating ENSO behavior. As found here, and confirmed by a linear dynamical analysis, eastward-propagating SST anomalies become prevalent in ITF$_{clsd}$

(Fig. 7), which indicates a more dominant thermocline feedback mechanism relative to the local feedback processes. A decomposition of the lag correlations between the TNI and Niño-3 shown in Fig. 7c into their warm and cold components suggests that the warm and cold anomalies both propagate eastward in ITF$_{clsd}$ (Fig. 13b). In ITF$_{open}$, in contrast, there is asymmetry in the SST zonal propagation, with eastward propagation that is largely due to warm events (Fig. 13a). This is consistent with that seen in the observed system, although what sets this asymmetry remains largely unknown (McPhaden and Zhang 2009). Existing theories (e.g., Fedorov and Philander 2001) have not taken this asymmetry into account, possibly because of the closed Pacific basin incorporated in their simpler models. It is possible that the existence of the ITF, perhaps coupled with the trade winds, sets up this fundamental asymmetry. This is an interesting topic for future research.

This study demonstrates how ENSO characteristics can be altered by first-order variations in the strength of the ITF. It is shown that ENSO feedback processes interact in competition with the mean climate, which is set to a large extent by the presence of the ITF. We have seen how changes in the ITF can establish the nature of ENSO variability at interannual-to-interdecadal time scales.

REFERENCES

An, S.-I., and B. Wang, 2000: Interdecadal change of the structure of the ENSO mode and its impact on the ENSO frequency. *J. Climate,* **13,** 2044–2055.

Ashok, K., S. K. Behera, S. A. Rao, H. Weng, and T. Yamagata, 2007: El Niño Modoki and its possible teleconnection. *J. Geophys. Res.,* **112,** C11007, doi:10.1029/2006JC003798.

Battisti, D. S., and A. C. Hirst, 1989: Interannual variability in the tropical atmosphere–ocean system: Influence of the basic state and ocean geometry. *J. Atmos. Sci.,* **46,** 1678–1712.

Bjerknes, J., 1969: Atmospheric teleconnections from the equatorial Pacific. *Mon. Wea. Rev.,* **97,** 163–172.

Bryan, K., S. Manabe, and R. C. Pacanowski, 1975: A global ocean–atmosphere climate model. Part II. The oceanic circulation. *J. Phys. Oceanogr.,* **5,** 30–46.

Burgers, G., and D. B. Stephenson, 1999: The ''normality'' of El Niño. *Geophys. Res. Lett.,* **26,** 1027–1030.

Cai, W., and T. Cowan, 2009: La Niña Modoki impacts Australia autumn rainfall variability. *Geophys. Res. Lett.,* **36,** L12805, doi:10.1029/2009GL037885.

——, G. Meyers, and G. Shi, 2005: Transmission of ENSO signal to the Indian Ocean. *Geophys. Res. Lett.,* **32,** L05616, doi:10.1029/2004GL021736.

Cane, M. A., and P. Molnar, 2001: Closing of the Indonesian seaway as a precursor to East African aridification around 3–4 million years ago. *Nature,* **411,** 157–162.

Capotondi, A., A. Wittenberg, and S. Masina, 2006: Spatial and temporal structure of tropical Pacific interannual variability in 20th century coupled simulations. *Ocean Modell.,* **15,** 274–298.

Cisewski, B., V. H. Strass, and H. Prandke, 2005: Upper-ocean vertical mixing in the Antarctic polar front zone. *Deep-Sea Res. II,* **52,** 1087–1108.

Collins, M., and Coauthors, 2010: El Niño and climate change. *Nat. Geosci.,* **3,** 391–397.

Duffy, P. B., J. Bell, C. Covey, and L. Sloan, 2000: Effect of flux adjustments on temperature variability in climate models. *Geophys. Res. Lett.,* **27,** 763–766.

England, M. H., and F. Huang, 2005: On the interannual variability of the Indonesian throughflow and its linkage with ENSO. *J. Climate,* **18,** 1435–1444.

——, M. Tomczak, and J. S. Godfrey, 1992: Water-mass formation and Sverdrup dynamics: A comparison between climatology and a coupled ocean–atmosphere model. *J. Mar. Syst.,* **3,** 279–306.

Fedorov, A. V., and S. G. Philander, 2001: A stability analysis of tropical ocean–atmosphere interactions: Bridging measurements and theory for El Niño. *J. Climate,* **14,** 3086–3101.

——, P. S. Dekens, M. McCarthy, A. C. Ravelo, P. B. deMenocal, M. Barreiro, R. C. Pacanowski, and S. G. Philander, 2006: The Pliocene paradox (mechanisms for a permanent El Niño). *Science,* **312,** 1485–1489.

Feng, M., M. J. McPhaden, and T. Lee, 2010: Decadal variability of the Pacific subtropical cells and their influence on the southeast Indian Ocean. *Geophys. Res. Lett.,* **37,** L09606, doi:10.1029/2010GL042796.

Gargett, A. E., 1984: Vertical eddy diffusivity in the ocean interior. *J. Mar. Res.,* **42,** 359–393.

Gent, P. R., and J. C. McWilliams, 1990: Isopycnal mixing in ocean circulation models. *J. Phys. Oceanogr.,* **20,** 150–155.

——, J. Willebrand, T. J. McDougall, and J. C. McWilliams, 1995: Parameterizing eddy-induced tracer transports in ocean circulation models. *J. Phys. Oceanogr.,* **25,** 463–474.

Godfrey, J. S., 1989: A Sverdrup model of the depth-integrated flow for the World Ocean allowing for island circulations. *Geophys. Astrophys. Fluid Dyn.,* **45,** 89–112.

——, 1996: The effect of the Indonesian Throughflow on ocean circulation and heat exchange with the atmosphere: A review. *J. Geophys. Res.,* **101,** 12 217–12 237.

Gordon, A. L., 2005: Oceanography of the Indonesian Seas and their throughflow. *Oceanography,* **18,** 14–27.

Gordon, H. B., and Coauthors, 2002: The CSIRO Mk3 climate systems model. Tech. Rep. 60, CSIRO Atmospheric Research, 134 pp.

Gregory, D., and P. R. Rowntree, 1990: A mass flux convection scheme with representation of cloud ensemble characteristics and stability-dependent closure. *Mon. Wea. Rev.,* **118,** 1483–1506.

Guilyardi, E., 2006: El Niño–mean state seasonal cycle interactions in a multimodel ensemble. *Climate Dyn.,* **26,** 329–348.

——, A. Wittenberg, A. Fedorov, M. Collins, C. Wang, A. Capotondi, G. J. van Oldenborgh, and T. Stockdale, 2009: Understanding El Niño in ocean–atmosphere general circulation models: Progress and challenges. *Bull. Amer. Meteor. Soc.,* **90,** 325–340.

Hirst, A. C., and J. S. Godfrey, 1993: The role of Indonesian Throughflow in a global ocean GCM. *J. Phys. Oceanogr.,* **23,** 1057–1086.

——, S. P. O'Farrell, and H. B. Gordon, 2000: Comparison of a coupled ocean–atmosphere model with and without oceanic eddy-induced advection. Part I: Ocean spinup and control integrations. *J. Climate,* **13,** 139–163.

Jin, F.-F., 1997: An equatorial ocean recharge paradigm for ENSO. Part I: Conceptual model. *J. Atmos. Sci.,* **54,** 811–829.

——, S. T. Kim, and L. Bejarano, 2006: A coupled stability index for ENSO. *Geophys. Res. Lett.,* **33,** L23708, doi:10.1029/2006GL027221.

Jochum, M., B. Fox-Kemper, P. H. Molnar, and C. Shields, 2009: Differences in the Indonesian seaway in a coupled climate model and their relevance to Pliocene climate and El Niño. *Paleoceanography,* **24,** PA1212, doi:10.1029/2008PA001678.

Kang, I.-S., S.-I. An, and F.-F. Jin, 2001: A systematic approximation of the SST anomaly equation for ENSO. *J. Meteor. Soc. Japan,* **79,** 1–10.

Kirtman, B. P., 1997: Oceanic Rossby wave dynamics and the ENSO period in a coupled model. *J. Climate,* **10,** 1690–1704.

Knutson, T. R., and S. Manabe, 1995: Time-mean response over the tropical Pacific to increased CO_2 in a coupled ocean–atmosphere model. *J. Climate,* **8,** 2181–2199.

Koutavas, A., J. Lynch-Stieglitz, T. M. Marchitto Jr., and J. P. Sachs, 2002: El Niño-like pattern in ice age tropical Pacific sea surface temperature. *Science,* **297,** 226–230.

Kowalczyk, E. A., J. R. Garratt, and P. B. Krummel, 1994: Implementation of a soil-canopy scheme into the CSIRO GCM—Regional aspects of the model response. Tech. Rep. 32, CSIRO Division of Atmospheric Research, 59 pp.

Kuhnt, W., A. Holbourn, R. Hall, M. Zuvela, and R. Käse, 2004: Neogene history of the Indonesian Throughflow. *Continent–Ocean Interactions within East Asian Marginal Seas, Geophys. Monogr.,* Vol. 149, Amer. Geophys. Union, 299–320.

Lea, D. W., D. K. Pak, and H. J. Spero, 2000: Climate impact of late quaternary equatorial Pacific sea surface temperature variations. *Science,* **289,** 1719–1724.

Lee, T., I. Fukumori, D. Menemenlis, Z. Xing, and L.-L. Fu, 2002: Effects of the Indonesian Throughflow on the Pacific and Indian Oceans. *J. Phys. Oceanogr.,* **32,** 1404–1429.

McPhaden, M. J., and D. Zhang, 2002: Slowdown of the meridional overturning circulation in the upper Pacific Ocean. *Nature,* **415,** 603–608.

——, and X. Zhang, 2009: Asymmetry in zonal phase propagation of ENSO sea surface temperature anomalies. *Geophys. Res. Lett.,* **36,** L13703, doi:10.1029/2009GL038774.

——, S. E. Zebiak, and M. H. Glantz, 2006: ENSO as an integrating concept in earth science. *Science,* **314,** 1739–1745.

Meinen, C. S., and M. J. McPhaden, 2000: Observations of warm water volume changes in the equatorial Pacific and their relationship to El Niño and La Niña. *J. Climate,* **13,** 3551–3559.

Meyers, G., 1996: Variation of Indonesian Throughflow and ENSO. *J. Geophys. Res.,* **101,** 12 255–12 264.

Neelin, J. D., and I. M. Held, 1987: Modeling tropical convergence based on the moist static energy budget. *Mon. Wea. Rev.,* **115,** 3–12.

——, D. S. Battisti, A. C. Hirst, F.-F. Jin, Y. Wakata, T. Yamagata, and S. E. Zebiak, 1998: ENSO theory. *J. Geophys. Res.,* **103,** 14 261–14 290.

O'Farrell, S. P., 1998: Investigation of the dynamic sea ice component of a coupled atmosphere–sea ice general circulation model. *J. Geophys. Res.,* **103,** 15 751–15 782.

Phipps, S. J., 2010: The CSIRO Mk3L climate system model v1.2. Antarctic Climate and Ecosystems Cooperative Research Centre Tech. Rep., 121 pp.

Pierce, D. W., T. P. Barnett, and U. Mikolajewicz, 1995: Competing roles of heat and freshwater fluxes in forcing thermohaline oscillations. *J. Phys. Oceanogr.,* **25,** 2046–2064.

Potemra, J. T., 1999: Seasonal variations of upper-ocean transport from the Pacific to the Indian Ocean via Indonesian Straits. *J. Phys. Oceanogr.,* **29,** 2930–2944.

——, and N. Schneider, 2007: Interannual variations of the Indonesian Throughflow. *J. Geophys. Res.,* **112,** C05035, doi:10.1029/2006JC003808.

Rodgers, K. B., M. Latif, and S. Legutke, 2000: Sensitivity of equatorial Pacific and Indian Ocean water masses to the position of the Indonesian Throughflow. *Geophys. Res. Lett.,* **27,** 2941–2944.

Rotstayn, L. D., B. F. Ryan, and J. J. Katzfey, 2000: A scheme for calculation of the liquid fraction in mixed-phase stratiform cloud in large-scale models. *Mon. Wea. Rev.,* **128,** 1070–1088.

Santoso, A., A. Sen Gupta, and M. H. England, 2010: Genesis of Indian Ocean mixed layer temperature anomalies: A heat budget analysis. *J. Climate,* **23,** 5375–5403.

Schneider, N., 1998: The Indonesian Throughflow and the global climate system. *J. Climate,* **11,** 676–689.

Schopf, P. S., and M. J. Suarez, 1988: Vacillations in a coupled ocean–atmosphere system. *J. Atmos. Sci.,* **45,** 549–566.

Shi, G., J. Ribbe, W. Cai, and T. Cowan, 2007: Multidecadal variability in the transmission of ENSO signals to the Indian Ocean. *Geophys. Res. Lett.,* **34,** L09706, doi:10.1029/2007GL029528.

Song, Q., G. A. Vecchi, and A. J. Rosati, 2007: The role of the Indonesian Throughflow in the Indo-Pacific climate variability in the GFDL coupled climate model. *J. Climate,* **20,** 2434–2451.

Taschetto, A. S., and M. H. England, 2009: El Niño Modoki impacts on Australian rainfall. *J. Climate,* **22,** 3167–3174.

Tillinger, D., and A. L. Gordon, 2009: Fifty years of the Indonesian Throughflow. *J. Climate,* **22,** 6342–6355.

Trenberth, K. E., and D. P. Stepaniak, 2001: Indices of El Nino evolution. *J. Climate,* **14,** 1697–1701.

Tudhope, A. W., and Coauthors, 2001: Variability in the El Niño–Southern Oscillation through a glacial–interglacial cycle. *Science,* **291,** 1511–1517.

Voris, H. K., 2000: Maps of Pleistocene sea levels in Southeast Asia: Shorelines, river systems, and time durations. *J. Biogeogr.,* **27,** 1153–1167.

Vranes, K., A. L. Gordon, and A. Ffield, 2002: The heat transport of the Indonesian Throughflow and implications for the Indian Ocean heat budget. *Deep-Sea Res. II,* **49,** 1391–1410.

Wainwright, L., G. Meyers, S. Wijffels, and L. Pigot, 2008: Change in the Indonesian Throughflow with the climatic shift of 1976/77. *Geophys. Res. Lett.,* **35,** L03604, doi:10.1029/2007GL031911.

Wajsowicz, R. C., 1993: The circulation of the depth-integrated flow around an island with application to the Indonesian Throughflow. *J. Phys. Oceanogr.,* **23,** 1470–1484.

——, and E. K. Schneider, 2001: The Indonesian Throughflow's effect on global climate determined from the COLA coupled climate system. *J. Climate,* **14,** 3029–3042.

Wang, W., and M. J. McPhaden, 2000: The surface layer heat balance in the equatorial Pacific Ocean. *J. Phys. Oceanogr.,* **30,** 2989–3008.

Wijffels, S. E., G. Meyers, and J. S. Godfrey, 2008: A 20-yr average of the Indonesian Throughflow: Regional currents and the interbasin exchange. *J. Phys. Oceanogr.,* **38,** 1965–1978.